Supplementary Information (SI) for Materials Horizons.
This journal is © The Royal Society of Chemistry 2026

Supporting Information

Bio-Derived Ionic Coacervate–Engineered Cellulose Liquid Crystal Films for Electrically Reconfigurable Microwave Absorption

Haoyuan Li,[a] *Yongjuan Wang,*[a] *Zhonghui Li,*[a] *Shuang Liang,*[a] *Yuming Zhou,*[a] *Wenhua Gao,*[b] *Man He* *[a]

[a] *Jiangsu Optoelectronic Functional Materials and Engineering Laboratory, School of Chemistry and Chemical Engineering, Southeast University, Nanjing 211189, China*

[b] *State Key Laboratory of Advanced Papermaking and Paper-based Materials, South China University of Technology, Guangzhou 510640, China*

Corresponding authors

* E-mail address: heman@seu.edu.cn (Man He)

Materials and Methods

Materials

(±)-Epichlorohydrin (ECH), N-methylimidazole, tin (IV) chloride ($SnCl_4$), trifluoroacetic acid (CF_3COOH), 1,4-butanediol (BDO), NaClO and ionic liquids 1-Methyl-3-octylimidazolium chloride ([OMIM][Cl]) were purchased from Aladdin. Ethylenediaminetetraacetic acid disodium salt (EDTA-2Na) was purchased from Sigma-Aldrich. 1,2-dichloroethane, chloroform, diethyl ether, methanol, and ethanol were purchased from Macklin Inc., and deionized (DI) water was made by Milli-Q Purification System. The cellulose nanocrystal (CNC) suspension (roughly 1.4 wt% solid content) was purchased from Tianjin Woodelf Biotechnology Co. Ltd, China, and were stored at 4 °C for further treatment.

Synthesis of PIL

The specific synthesis pathway is based on literature reports[1]. First, 25.0 mL 1,2-dichloroethane, 1.8 g BDO, 0.234 mL $SnCl_4$, and 0.613 mL CF_3COOH were added to a three-necked flask. Secondly, 121.2 g ECH was added dropwise to the flask with stirring in ice bath (0 ~ 5 °C) for 1 h. Afterward, the solution was kept stirring at 65 ~ 70 °C in nitrogen for another 3 h. Then, the reaction mixture was cooled to room temperature naturally, and 70.0 g aqueous 10% methanol solution containing 0.8 g EDTA-2Na was added to terminate the reaction. The organic phase was extracted and washed twice with 70.0 g of aqueous 10% methanol solution, and concentrated by rotary evaporation under reduced pressure at 70 °C. The remaining viscous solution

was vacuum-dried for 24 h at 90 °C. Poly-Epichlorohydrin (PECH) was obtained through the abovementioned ring-opening polymerization of ECH (**Figure S1**).

Poly(ionic liquid) (PIL), as a novel class of polyelectrolytes, consist of polymeric backbones with ionic liquid (IL) species in the repeating unit. PILs with imidazolium-based cation as side groups were prepared by quaternization reaction of PECH and N-methylimidazole with a Cl: N-methylimidazole molar ratio of 2:3. The prepared PECH and N-methylimidazole (1.33 times the mass of PECH) were added into the flask and mechanically stirred in nitrogen for 24 h at 100 °C. Then, chloroform and diethyl ether were added in turn to wash excess N-methylimidazole. The filtered precipitate was rinsed several times with DI water until the concentration of chlorine ion Cl^- in the filtrate was below 5.0 mg L^{-1}. PIL was obtained after drying under vacuum at 60 °C for 24 h.

^{1}H NMR (400 MHz, $(CD_3)_2SO$) δ (ppm): 9.779 (s, H), 8.045 (s, H), 7.938~7.888 (d, H), 7.561 (s, H), 7.094 (s, H), 6.861 (s, H), 4.515 (s, H), 4.309 (s, H), 3.999 (s, 4H), 3.634 (s, 4H), 3.466 (s, 4H).

^{13}C NMR (101 MHz, $(CD_3)_2SO$) δ (ppm): 137.95, 137.56, 128.39, 123.37, 120.56, 76.69, 67.69, 56.07, 49.77, 39.88, 39.74, 39.58, 39.46, 35.97, 32.83, 18.62.

Fabrication of cellulose liquid crystal film (CLCF)

First, 20 g of CNC suspension (4 wt %) was poured into a Petri dish as a matrix after being stirred and shaken thoroughly because the suspension is a shear-thinning fluid. The ethanol solution of PIL (10 wt %) was gently and evenly dropped on the surface of the suspension with different mass ratios. The mixture was subsequently

sonicated for 1 min. Then, the ethanol solution of IL was added to the suspension in the same manner with various proportions, followed by sonicating for 1 min. Finally, the films were obtained by peeling off after drying under ambient conditions for at least 3 days and drying under a vacuum at 70 °C for 24 h.

Fabrication of CNC-PIL films

20 g of CNC suspension (4 wt %) was poured into a Petri dish as a matrix after being stirred and shaken thoroughly. Then, the ethanol solution of PIL was added to the CNC suspension with various proportions, followed by sonicating about 30 seconds. Lastly, the films were obtained by peeling off after drying under ambient conditions for at least 3 days. The prepared samples were defined as CNC-PIL.

Density functional theoretical calculations:

The adsorption calculations were performed using the DMol3 package[2]. The PBE functional with D2 dispersion correction was utilized. A DNP basis sets were used in the expansion of the Kohn-Sham orbitals and the orbital-confining cutoff radii were 4.4 Å. DSPP norm-conserving pseudopotentials were used employed to describe the cores of atoms. The calculations use $\sigma = 0.01$ eV of Fermi smearing and the boundary of the calculations is non-periodic. To ensure the normal operation of calculations, both PIL and CNC models are built using monomer molecules for calculations.

Electromagnetic Formula:

The electromagnetic parameters in the frequency range of 8-12 GHz (X-band) were measured by a vector network analyzer. As a microwave absorption (MA) material, reflection loss (RL), input impedance (Z_{in}) and attenuation constant (α) are the

important evaluation indexes. According to transmission line theory, *RL* and α can be calculated by the following formula[3-5]:

Based on the transmission line theory, the RL and Z_{in} values of CLCF are calculated by the complex permittivity (ε_r) and complex permeability (μ_r) by the following equations:

$$\boldsymbol{RL(dB) = -20lg|(Z_{in} - Z_0)/(Z_{in} + Z_0)|} \quad \text{(Equation S1)}$$

$$\boldsymbol{Z_{in} = Z_0(\mu_r/\varepsilon_r)^{1/2}\tanh\left(j\frac{2\pi fd}{c}(\mu_r\varepsilon_r)^{1/2}\right)} \quad \text{(Equation S2)}$$

Where Z_{in} is the normalized input impedance of MA materials, Z_0 is the free space impedance; $\boldsymbol{\varepsilon_r}$ and $\boldsymbol{\mu_r}$ represent complex permittivity and complex permeability, respectively; *d* is the thickness of the MA materials; *f* is the frequency of microwave.

The attenuation constant (α) can be calculated through

$$\boldsymbol{\alpha = \frac{\sqrt{2}\pi f}{c}\sqrt{(\mu''\varepsilon'' - \mu'\varepsilon') + \sqrt{(\mu'\varepsilon'' + \mu''\varepsilon')^2 + (\mu''\varepsilon'' - \mu'\varepsilon')^2}}} \quad \text{(Equation S3)}$$

According to Debye theory, the relatively complex permittivity imaginary part (ε'') could be divided into conduction loss (ε_c'') and polarization loss (ε_p'') as following equations[6-8]:

$$\boldsymbol{\varepsilon'' = \frac{\omega\tau(\varepsilon_s - \varepsilon_\infty)}{1+\omega^2\tau^2} + \frac{\sigma}{\omega\varepsilon_0} = \varepsilon_p'' + \varepsilon_c''} \quad \text{(Equation S4)}$$

$$\boldsymbol{\varepsilon_c'' = \frac{\sigma}{\omega\varepsilon_0}} \quad \text{(Equation S5)}$$

where ω is angular frequency, $\boldsymbol{\varepsilon_s}$ is static dielectric constant, $\boldsymbol{\tau}$ is polarization relaxation time, $\boldsymbol{\varepsilon_\infty}$ is relative permittivity at high frequency and $\boldsymbol{\sigma}$ is electrical conductivity.

One Debye relaxation process corresponds to one semicircle (Cole-Cole semicircle) in accordance with Debye theory.

$$\left(\varepsilon' - \frac{\varepsilon_s+\varepsilon_\infty}{2}\right)^2 + (\varepsilon'')^2 = \left(\frac{\varepsilon_s-\varepsilon_\infty}{2}\right)^2 \qquad \text{(Equation S6)}$$

RCS Simulation：

For evaluating the practical application of the three samples, further simulation was carried out based on far-field response using Computer Simulation Technology (CST) Studio Suite 2024. In this simulation, the tested model consists of the upper absorber layer and the bottom perfect electric conductor (PEC) layer, where the size of the square was 100 mm * 100 mm, the thickness of the absorber layer was x mm (x corresponds to the thickness of RL_{min} for each set of samples), and the thickness of the bottom perfectly conducting layer (PEC) was set to 1.0 mm. The linearly polarized plane wave was defined as the excitation port, and the microwave propagates in the negative direction of the y-axis and the electric polarization direction is along the z-axis. The open (add space) boundary conditions were used in all directions. The scattering direction was determined by θ and φ. The radar cross section (RCS) of the simulated sample is expressed by the following equation[9-11].

$$\sigma(dBm^2) = 10log\left[\frac{4\pi S}{\lambda^2}\left|\frac{E_s}{E_i}\right|^2\right] \qquad \text{(Equation S7)}$$

where S is the area of the simulated plate, λ is the length of the incident microwave, E_s is the electric field intensity of transmitting waves, and E_i is the electric field intensity of receiving wave.

Supplementary Figures

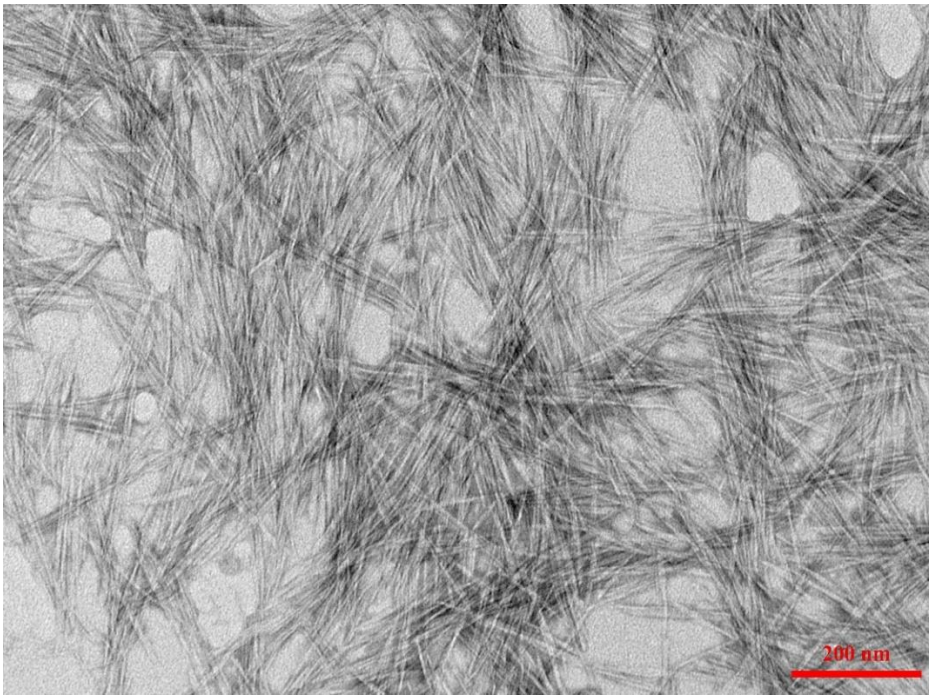

Figure S1. TEM images of CNC.

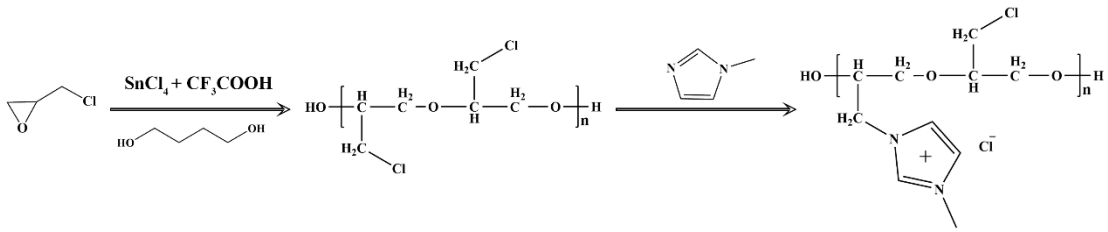

Figure S2. Synthetic procedure of PIL.

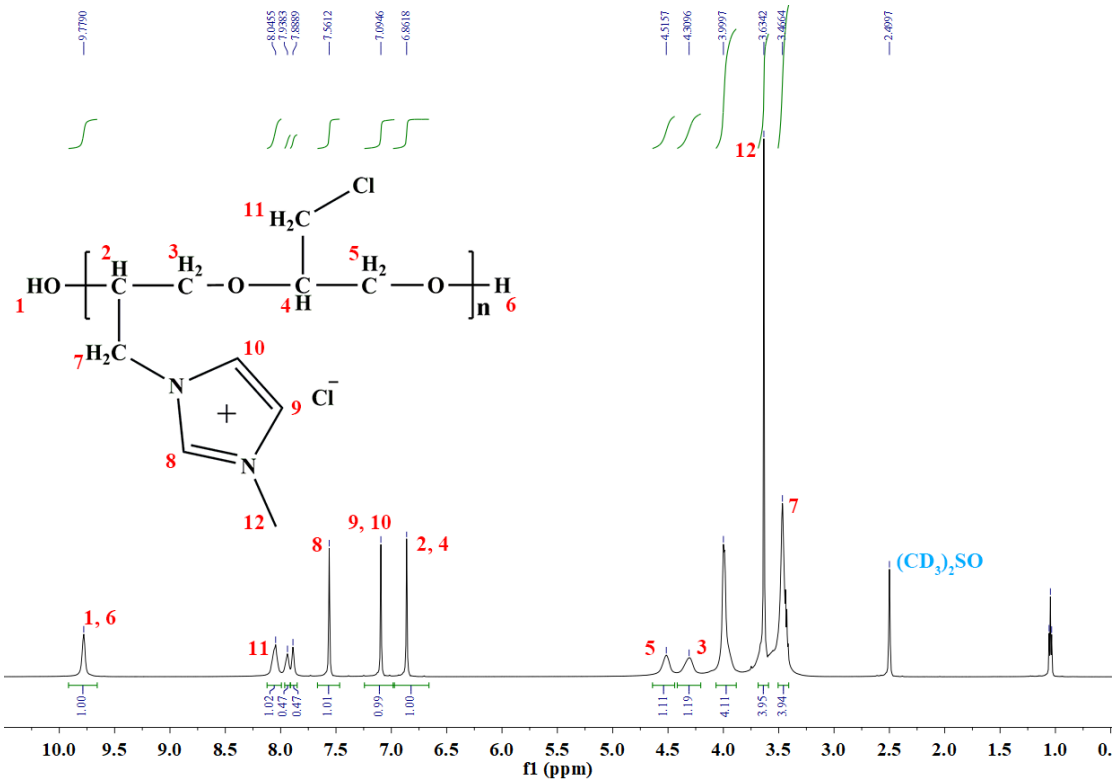

Figure S3. The ^{1}H NMR spectra of PIL.

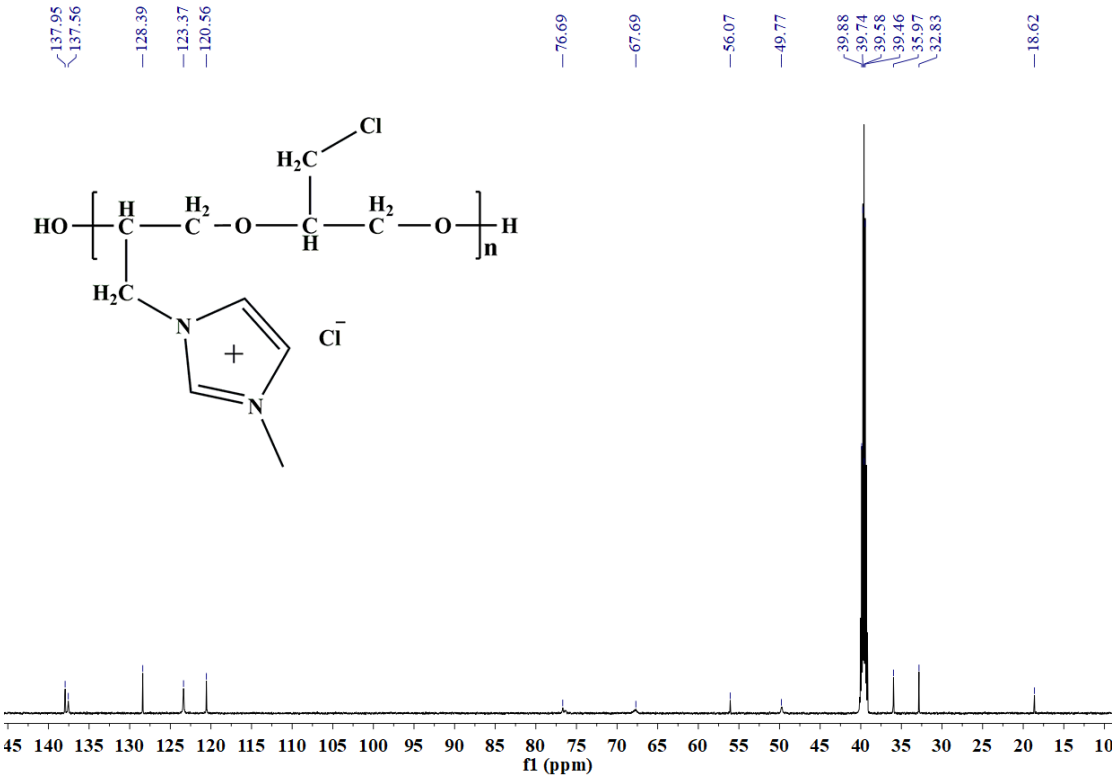

Figure S4. The ^{13}C NMR spectra of PIL.

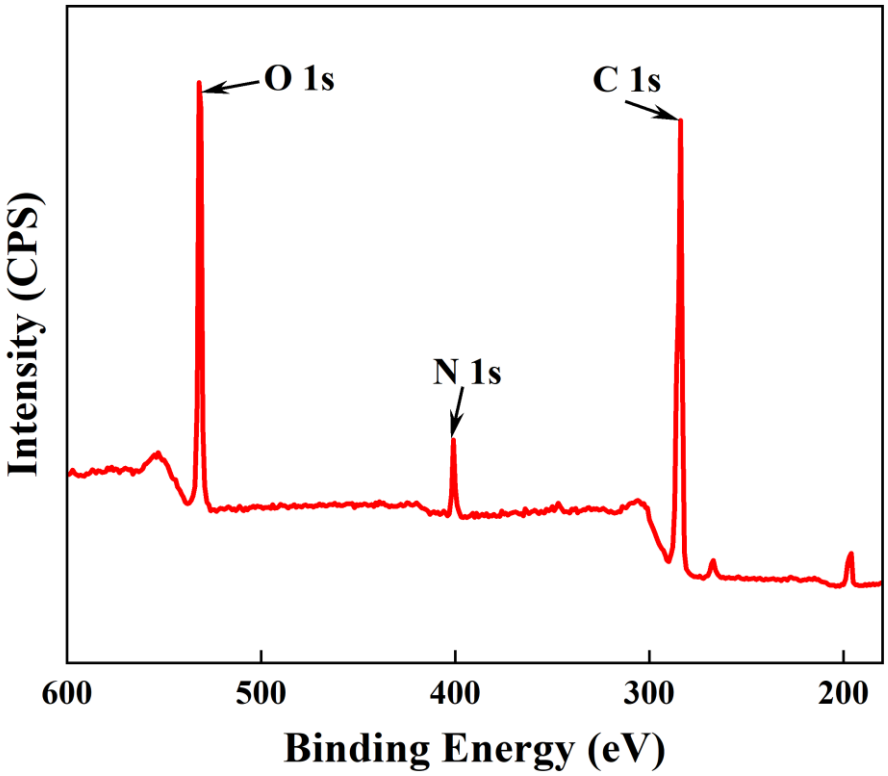

Figure S5. The wide-scan XPS spectra of the PIL.

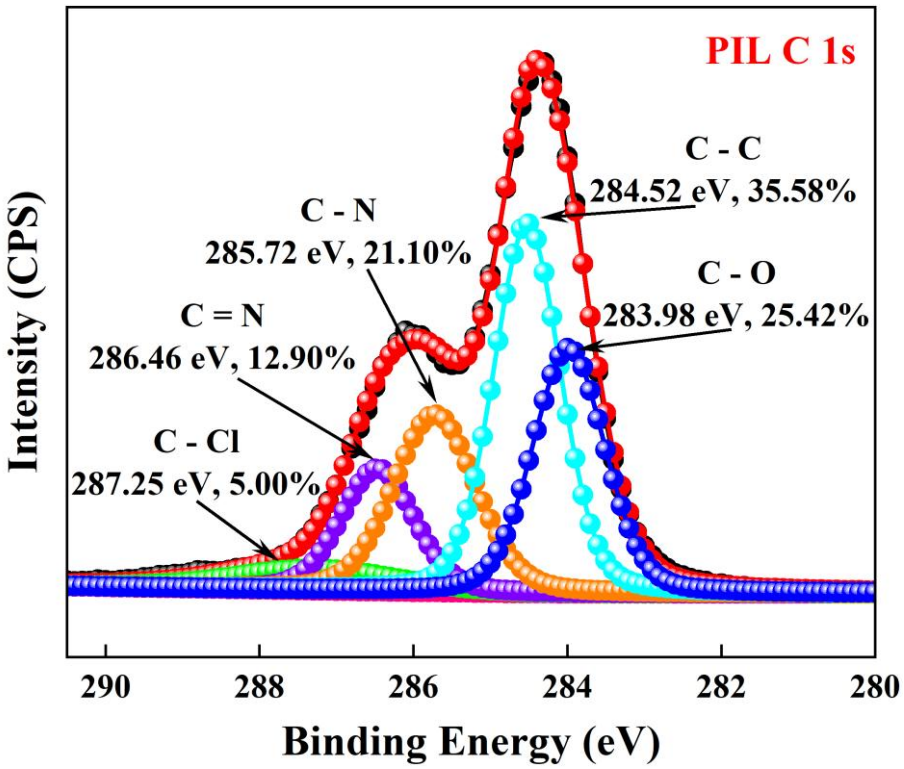

Figure S6. The C 1s XPS spectra of the PIL.

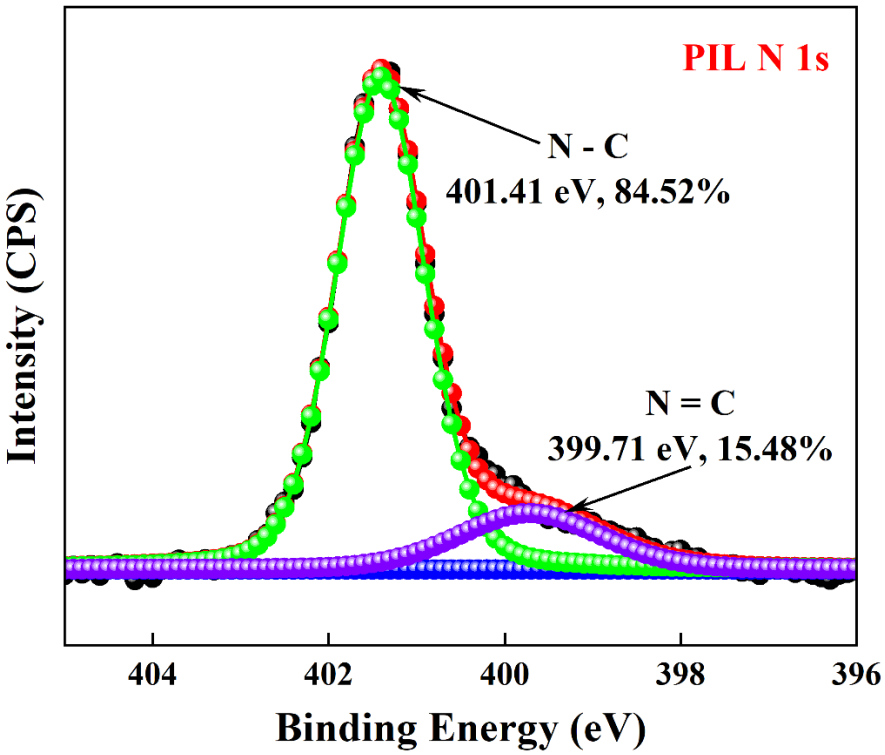

Figure S7. The N 1s XPS spectra of the PIL.

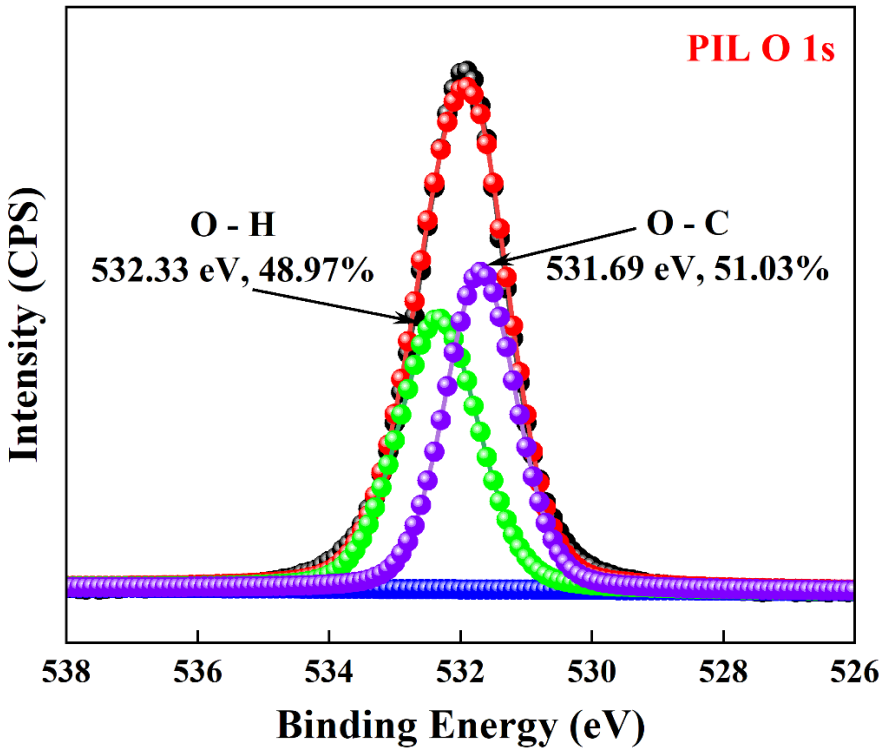

Figure S8. The O 1s XPS spectra of the PIL.

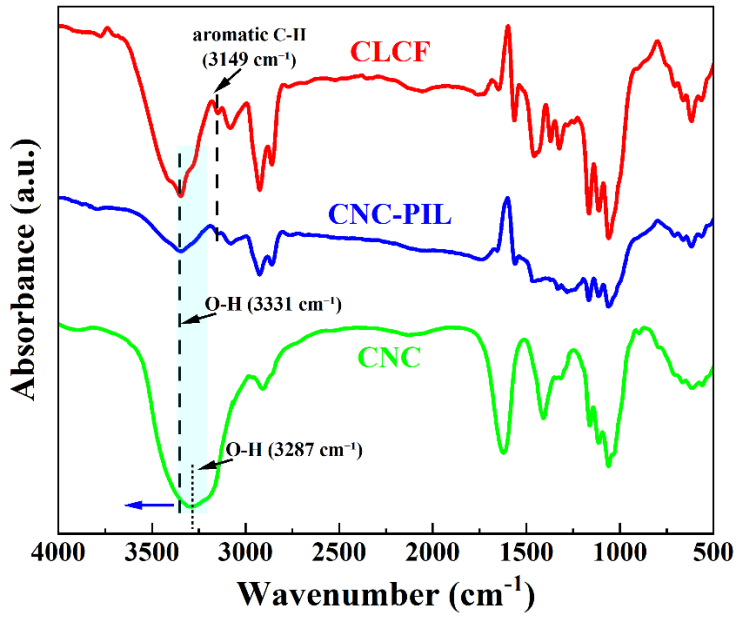

Figure S9. FTIR spectra of CNC, CNC-PIL, and CLCF.

A distinct absorption peak at 3149 cm^{-1}, corresponding to the aromatic C-H stretching vibration, appears in both CNC-PIL and CLCF but is absent in pristine CNC, confirming the successful incorporation of imidazolium cations.

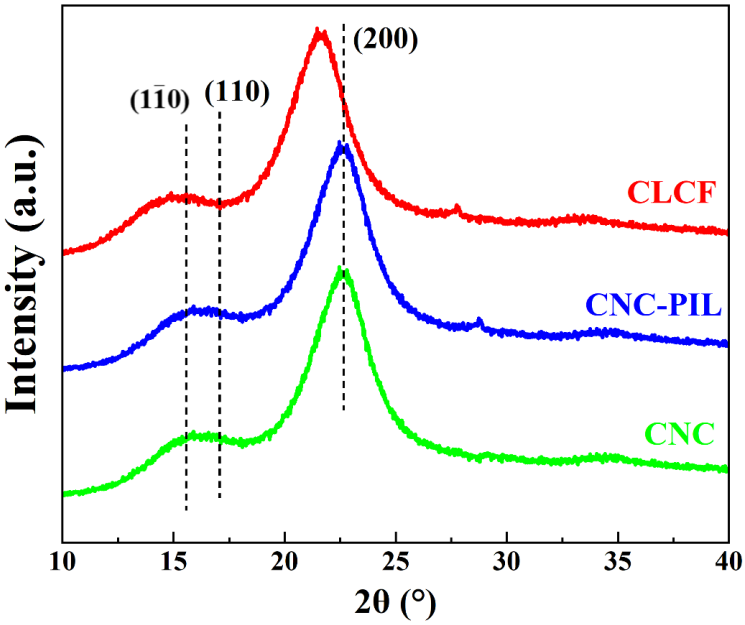

Figure S10. XRD patterns of CNC, CNC-PIL, and CLCF.

The CNC exhibits the clear diffraction peaks at 15.15°, 16.86°, and 22.63°, which are assigned to the (1$\bar{1}$0), (110), and (200) planes, respectively, confirming a typical cellulose I crystalline phase (green curve).

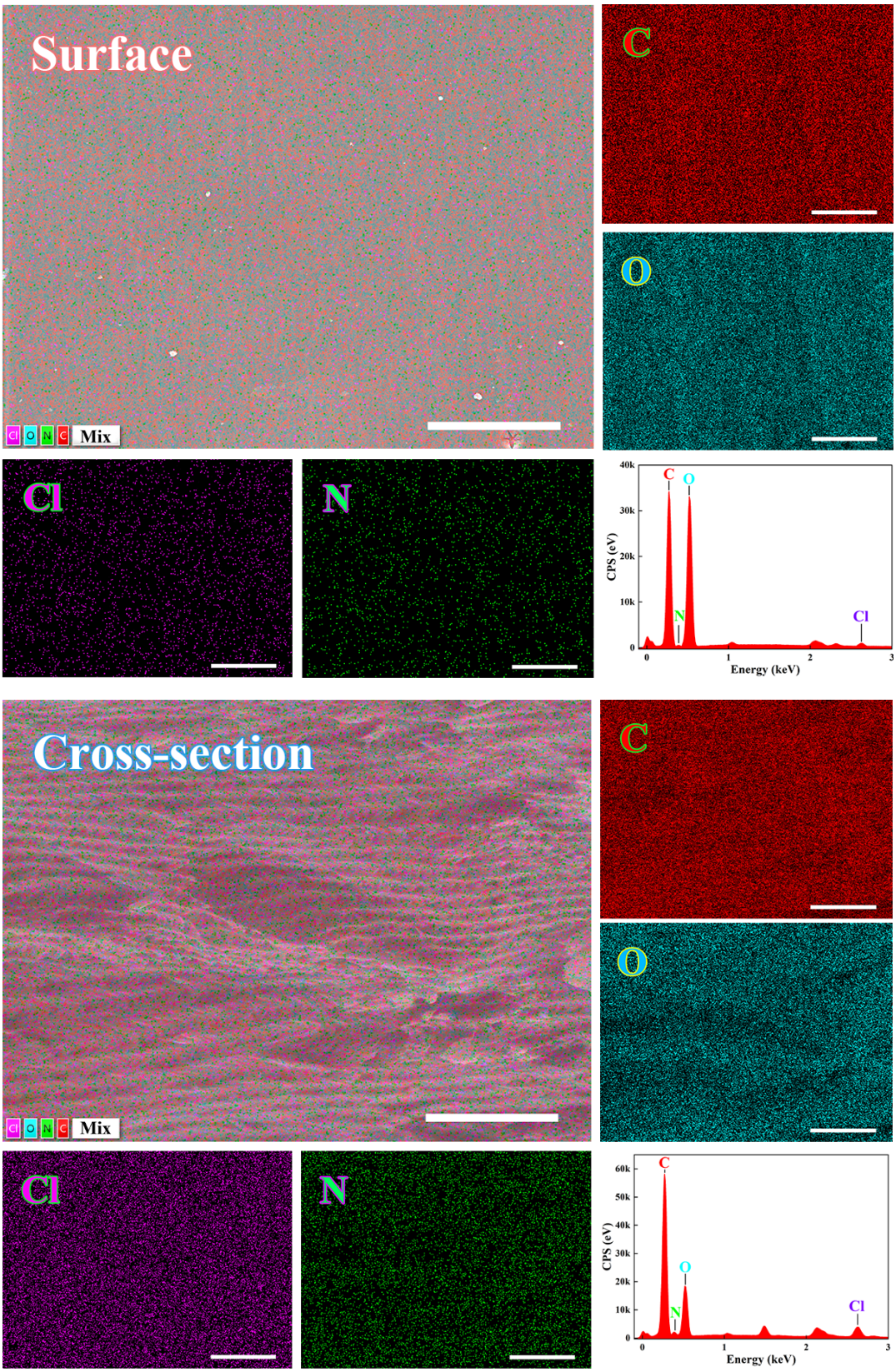

Figure S11. SEM images of CLCF surface and cross-section, and corresponding elemental mapping images.

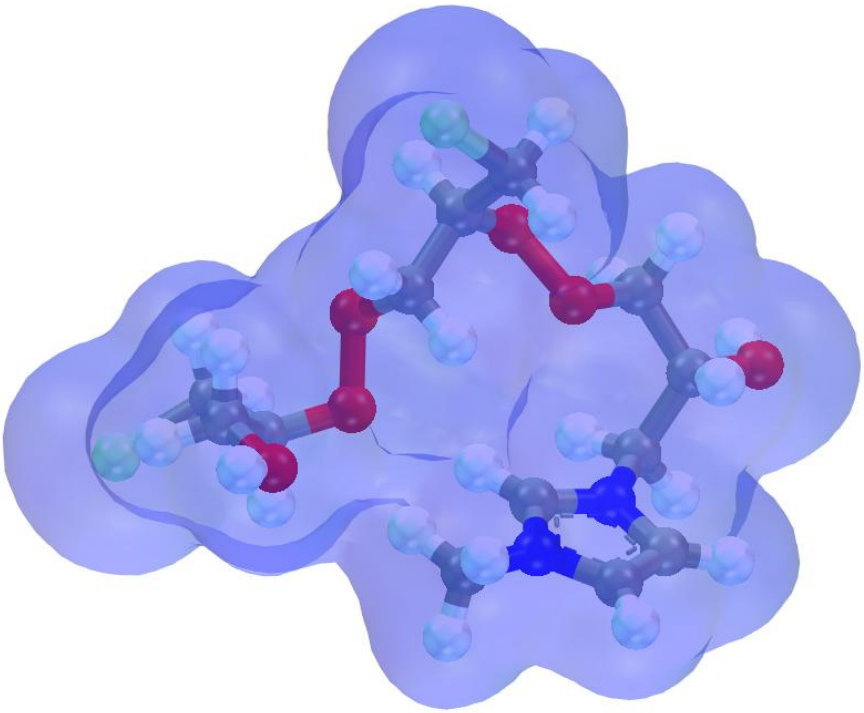

Figure S12. Surface electron cloud density of PIL.

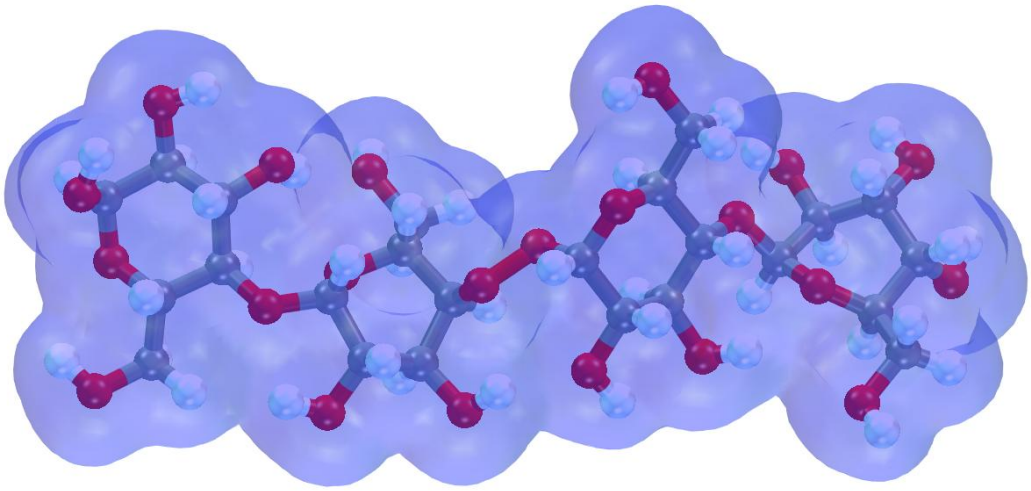

Figure S13. Surface electron cloud density of CNC.

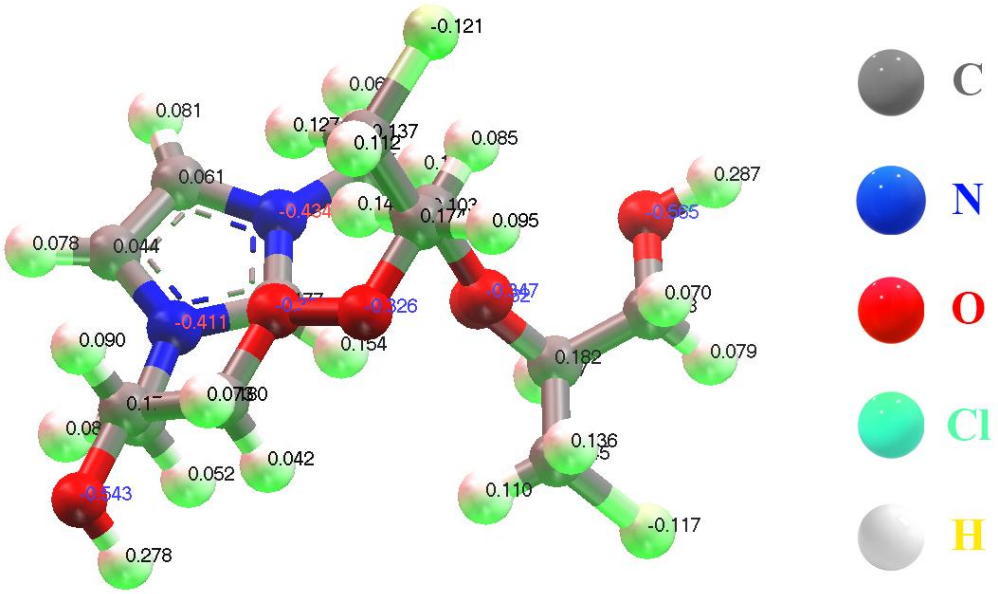

Figure S14. Single point energy calculation of PIL.

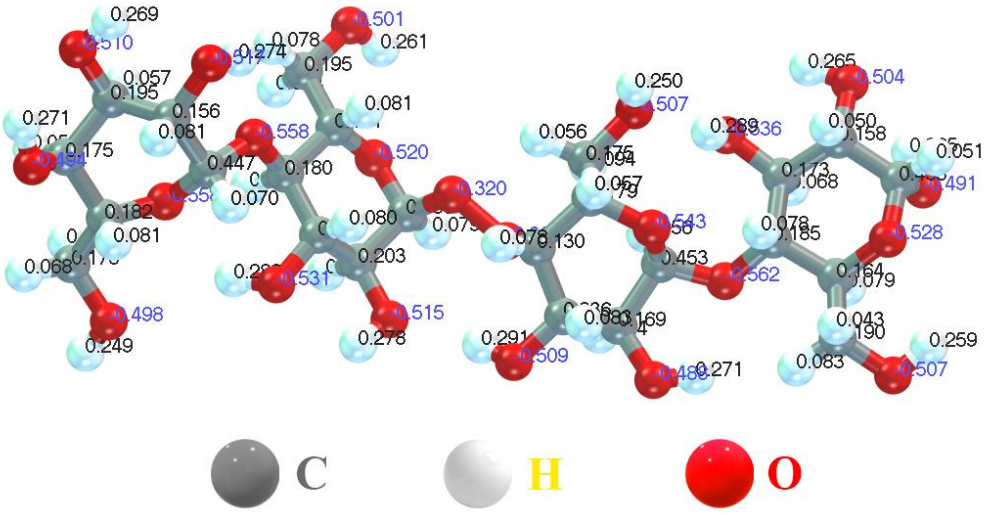

Figure S15. Single point energy calculation of CNC.

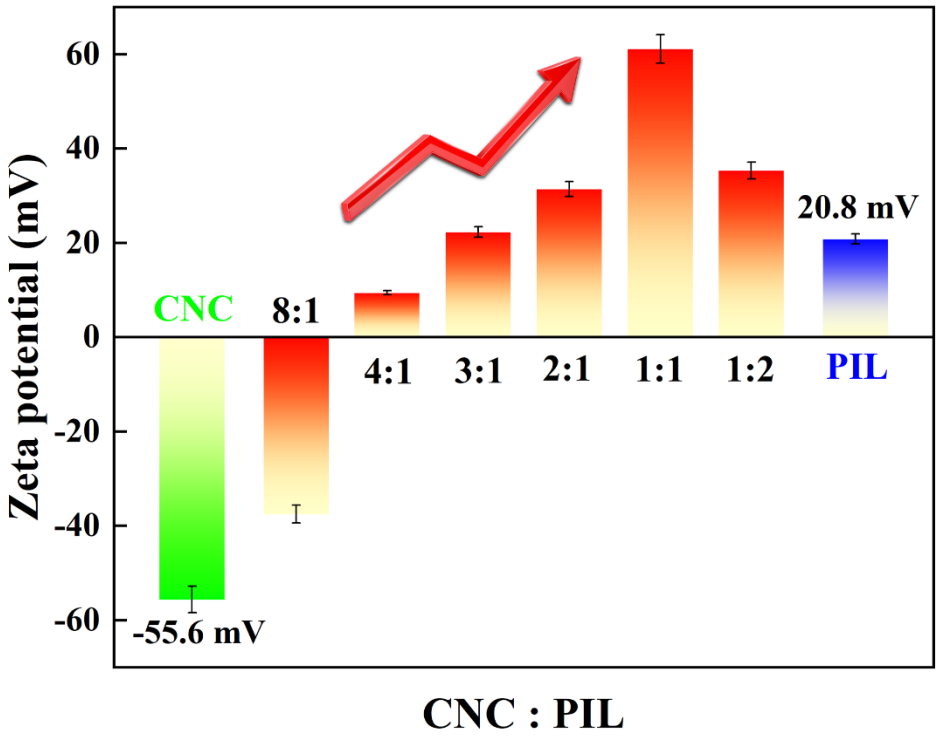

Figure S16. Zeta potentials of CNC dispersion, PIL solution, and their mixtures.

Zeta potential measurements were performed on dilute dispersions of CNC, PIL, and their mixtures. The gradual addition of PIL neutralizes the surface charges of CNC, with the Zeta potential shifting from negative to positive. At a mass ratio of CNC:PIL=4:1, sufficient PIL is adsorbed onto CNC to reverse its surface potential.

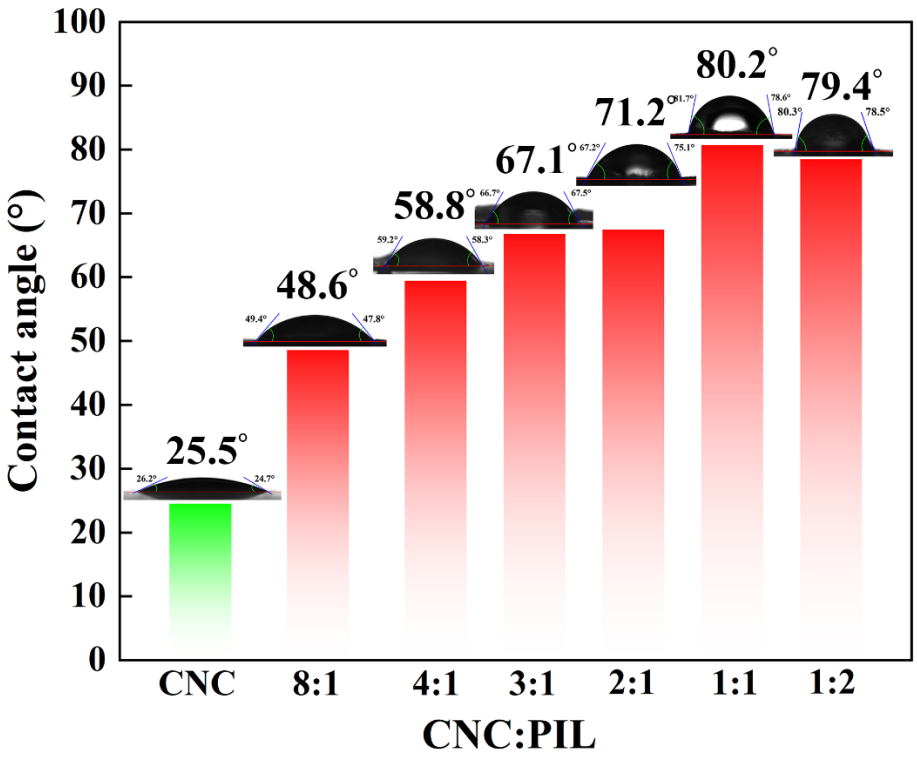

Figure S17. Water contact angle results of CNC dispersion, PIL solution, and their mixtures.

The water contact angles of the CNC-PIL films increase progressively with rising PIL content, and this enhancement indicates that the introduction of PIL effectively reduces the surface energy of the films, thereby improving their water resistance.

Figure S18. Photographs of CNC film.

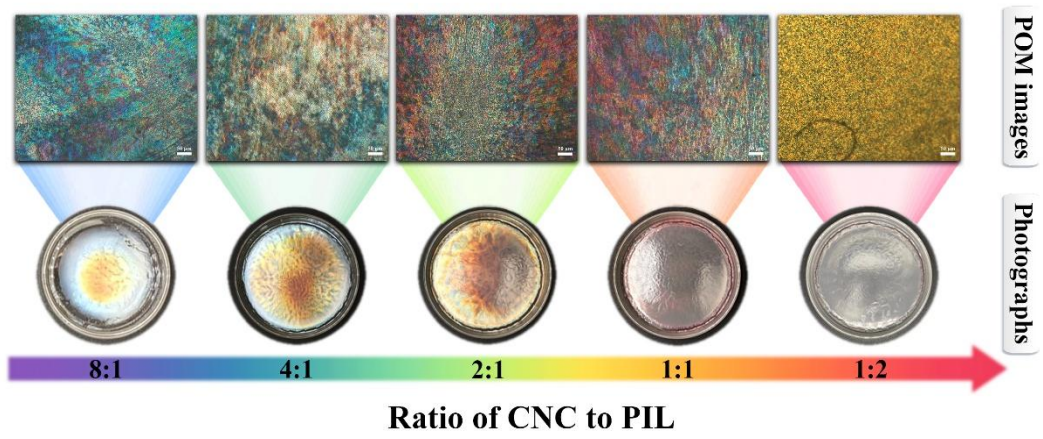

Figure S19. POM images and optical photographs of CNC-PIL films (scale bar is 50 μm).

CNC-PIL films show a color transition from iridescent rainbow to bright red as the mass ratio of PIL gradually increases. The progressive red-shift and eventual disappearance of structural color with further increasing PIL content arise from the pitch expansion of the cholesteric structure beyond the visible range. However, characteristic liquid crystal textures and fingerprint patterns remain observable under polarized light (top), indicating the persistence of the cholesteric phase.

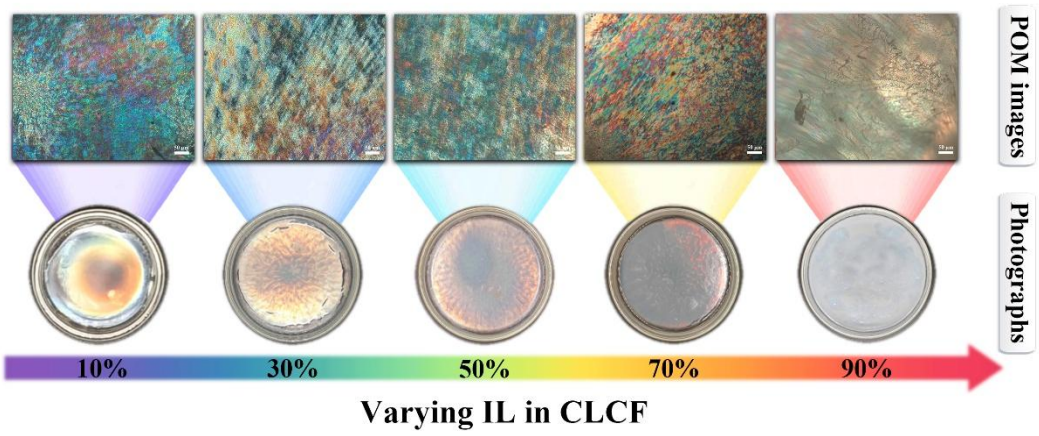

Figure S20. POM images and optical photographs of CLCF (scale bar is 50 μm).

The optical photographs (bottom) display a gradual transition in structural color from rainbow to bright red with increasing IL content. However, when the IL weight fraction reaches 70 wt%, the characteristic structural color of the liquid crystal nearly vanishes. At 90 wt% IL, the fingerprint textures of the cholesteric phase become barely discernible under polarized light (top). This behavior can be attributed to the penetration of IL into CNC domains, which disrupts the intermolecular hydrogen-bonding network and irreversibly damages the cholesteric liquid crystalline architecture.

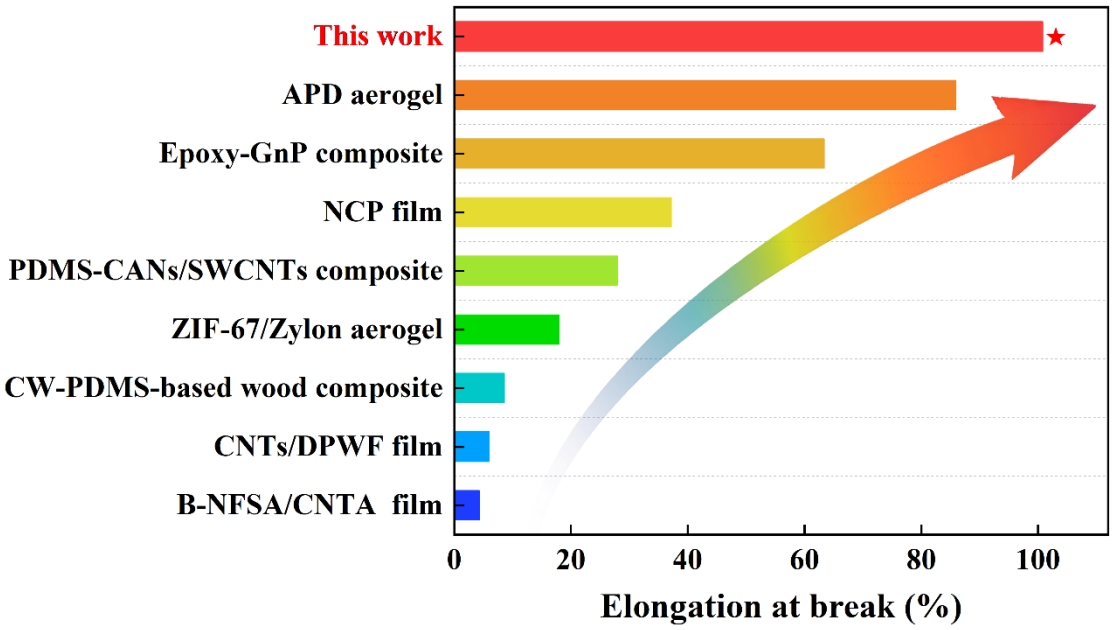

Figure S21. Comparison of elongation at break between CLCF and other flexible synthetic materials.[12-19]

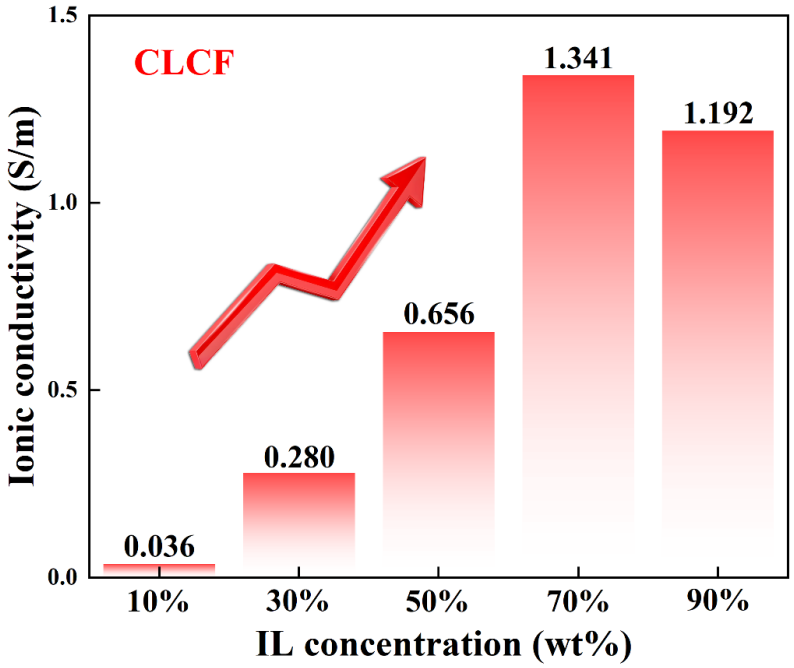

Figure S22. Ionic conductivity of the CLCF with varying IL weight fractions.

The ionic conductivity exhibits an upward trend with increasing IL content and then slightly declined at higher IL loadings. This is consistent with the trend shown in the open circuit voltage (V_{OC}) results of CLCF.

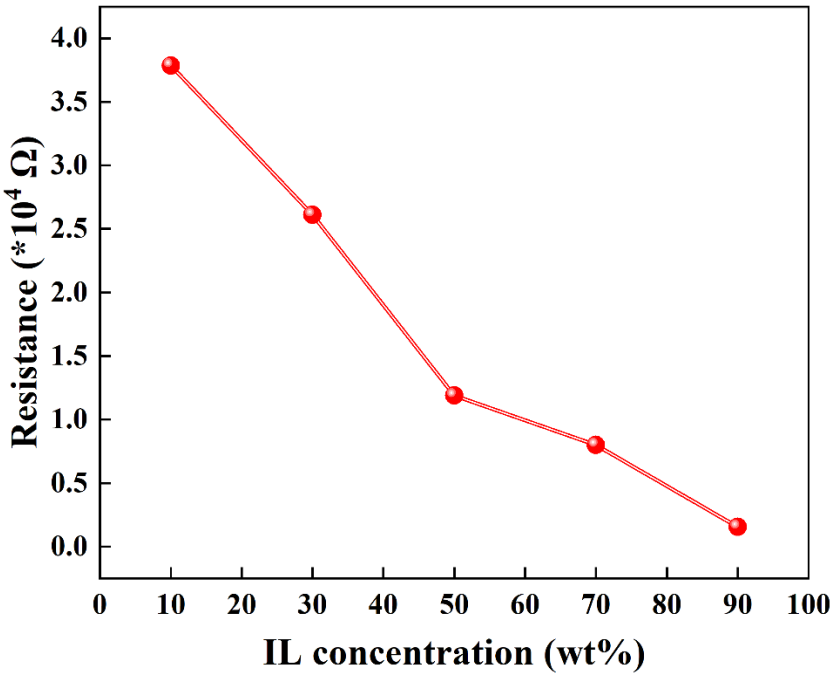

Figure S23. Resistance of CLCF with varying IL weight fractions.

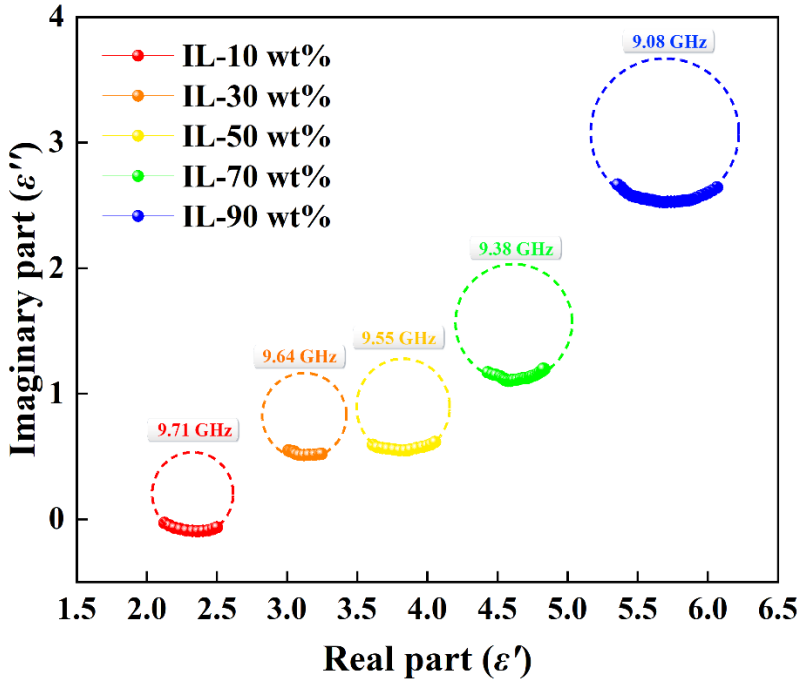

Figure S24. Cole–Cole curves of CLCF with varying IL weight fractions.

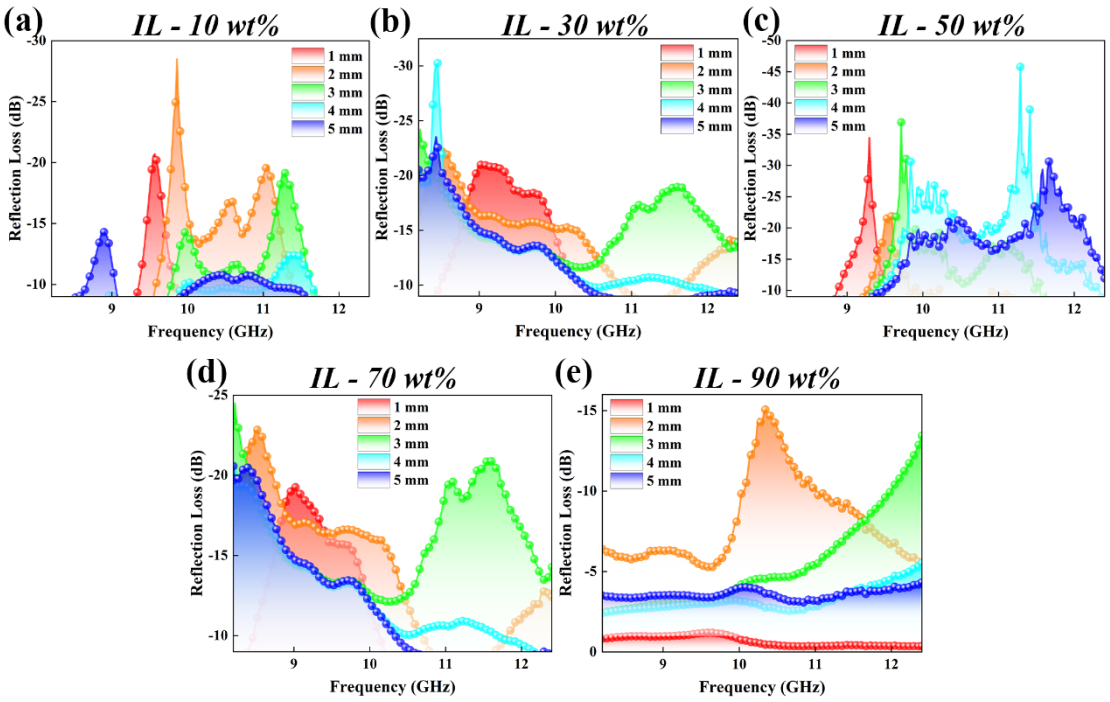

Figure S25. RL curves of CLCF with different thicknesses at varying IL weight fractions.

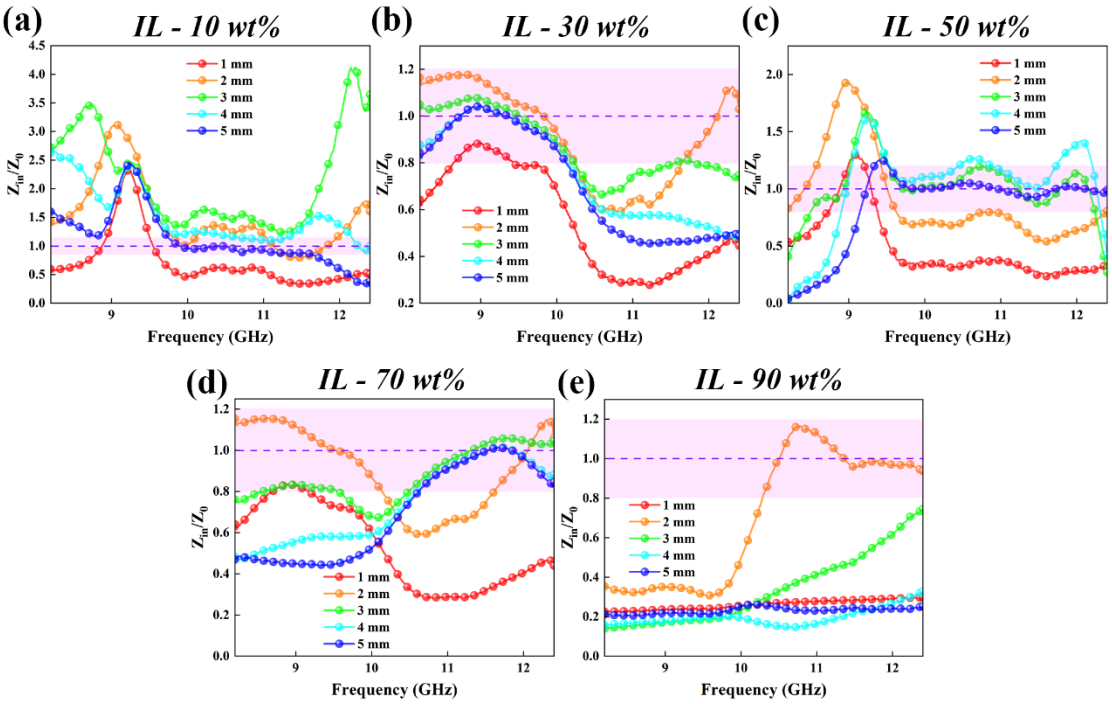

Figure S26. $|Z_{in}/Z_0|$ values of CLCF with different thicknesses at varying IL weight fractions.

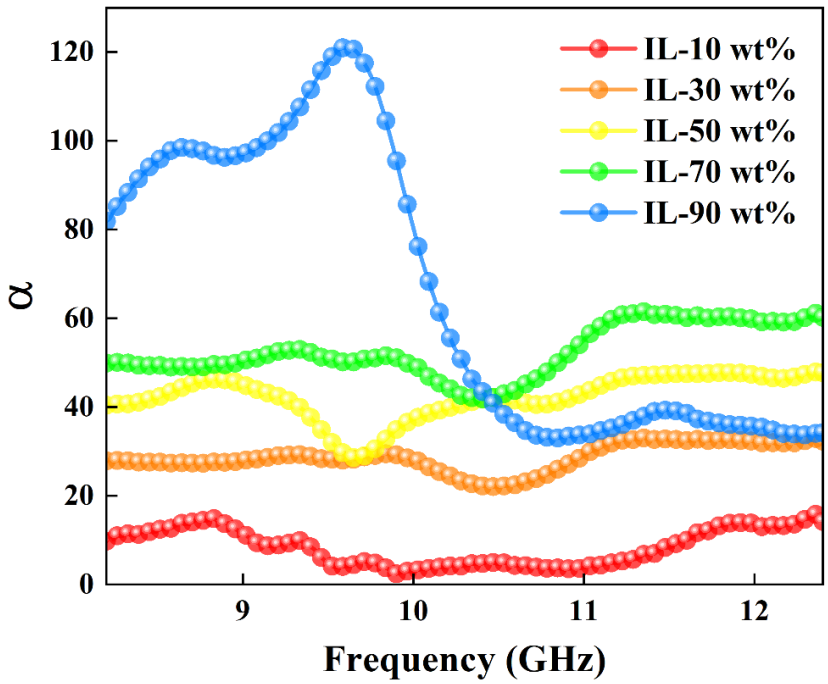

Figure S27. Attenuation constant α of CLCF with varying IL weight fractions.

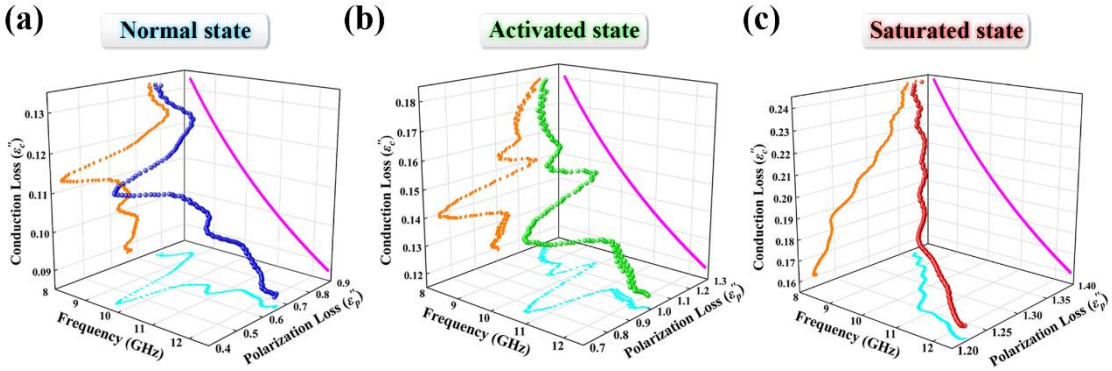

Figure S28. ε_c'' and ε_p'' of CLCF in (a) normal, (b) activated, and (c) saturated states.

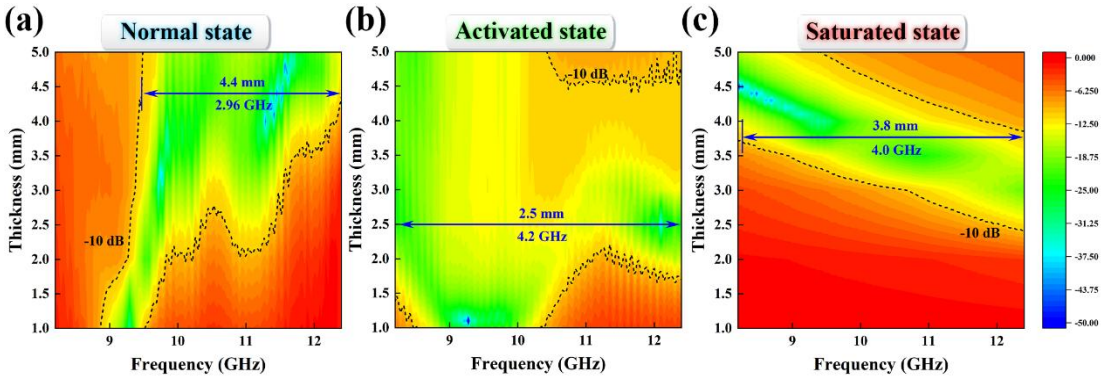

Figure S29. Two-dimensional (2D) RL contour plots of CLCF showing EAB performance in (a) normal, (b) activated, and (c) saturated states.

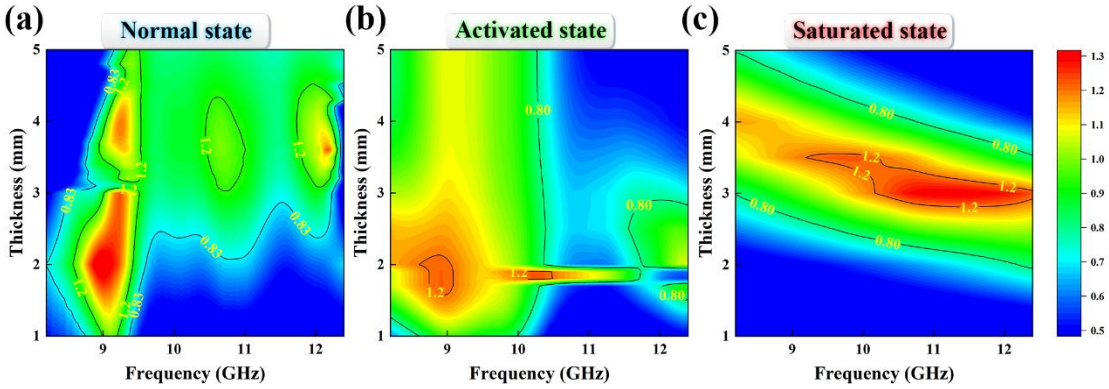

Figure S30. $|Z_{in}/Z_0|$ values of CLCF in (a) normal, (b) activated, and (c) saturated states.

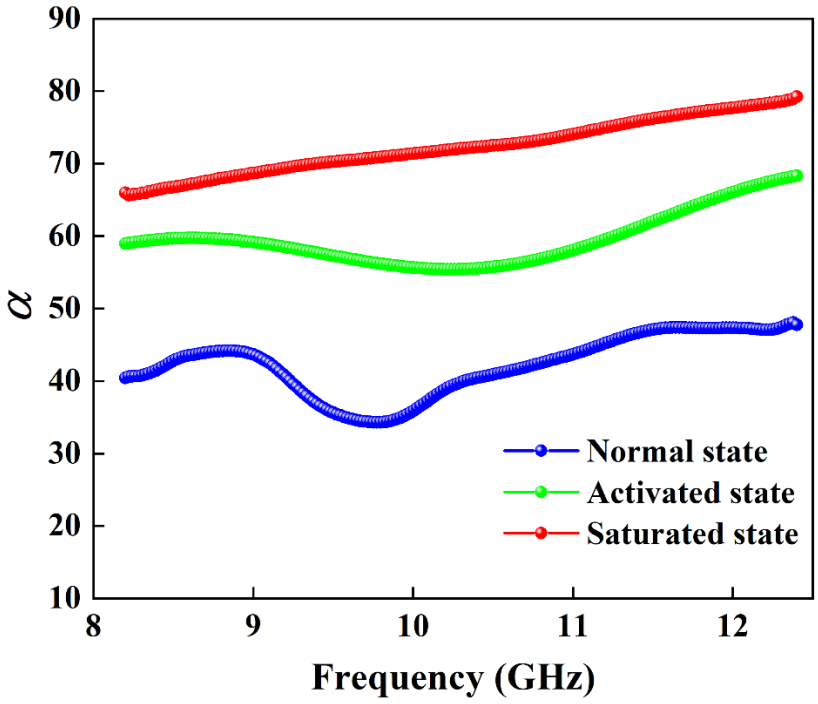

Figure S31. Attenuation constant α of CLCF in normal, activated, and saturated states.

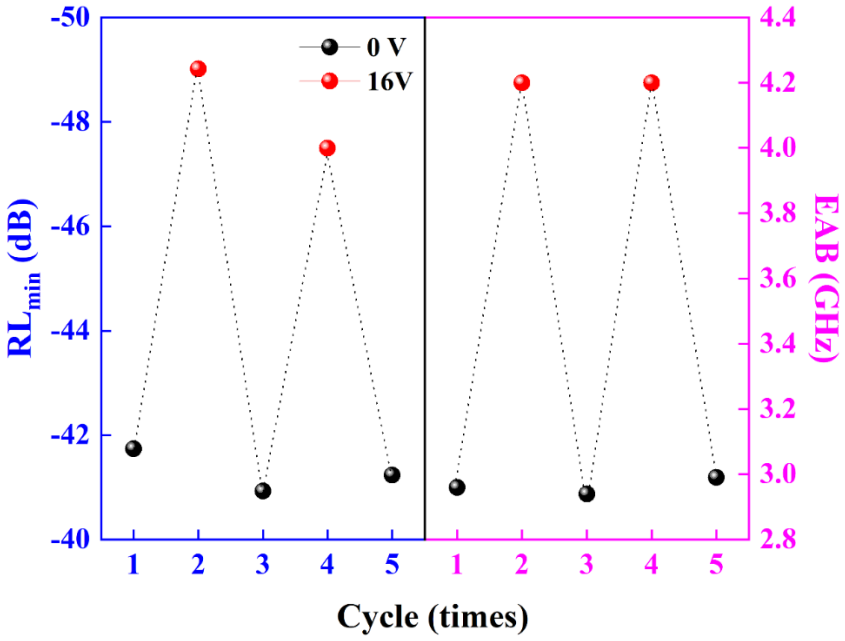

Figure S32. Reversible MA performance of CLCF under alternating 0 V/16 V cycles.

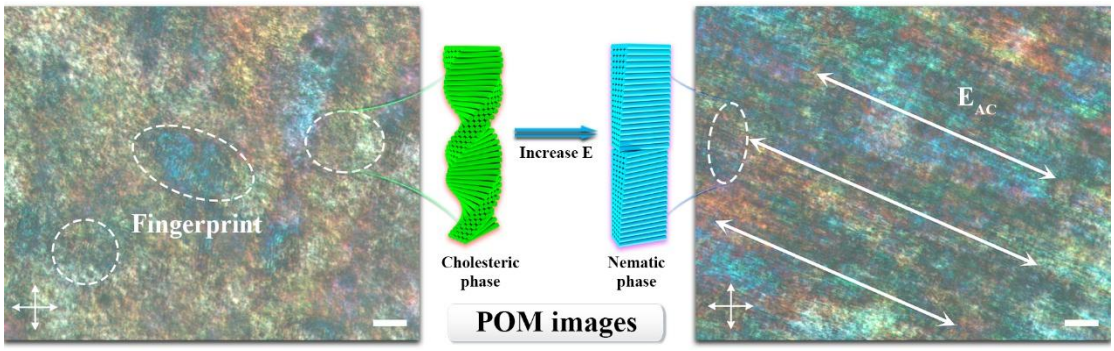

Figure S33. POM images of CLCF without stimulation and after 16V stimulation (scale bar is 5 μm).

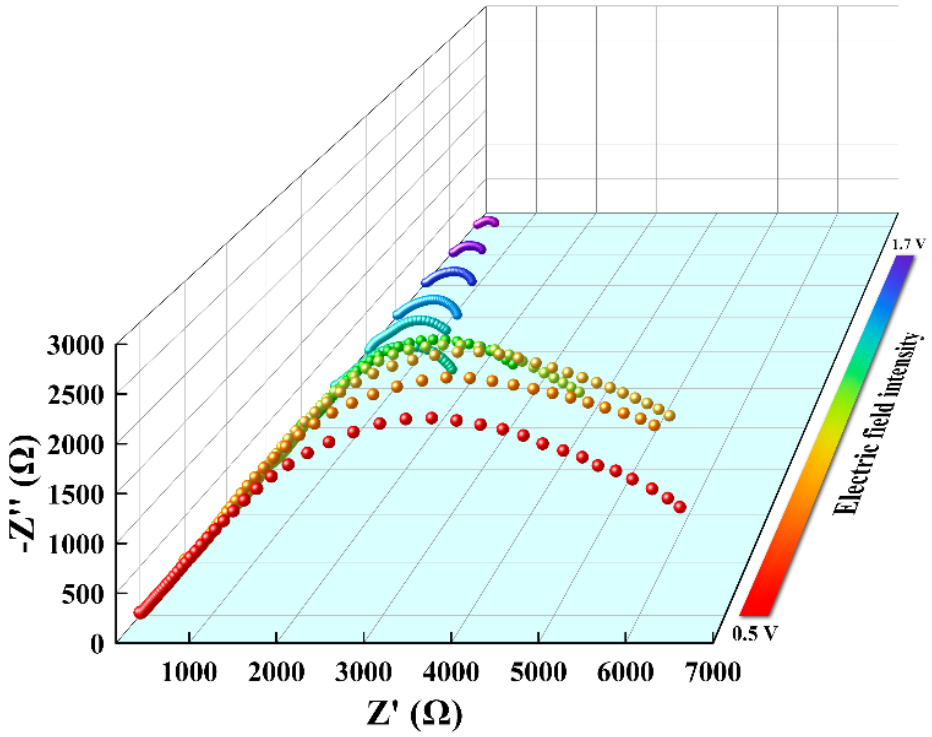

Figure S34. EIS plots of CLCF with gradient voltage.

References

1. X. Li, D. Lv, L. Ai, X. Wang, X. Xu, M. Qiang, G. Huang and X. Yao, *ACS Nano*, 2024, **18**, 12970-12980.
2. B. Delley, *Journal of Physical Chemistry*, 1996, **15**, 6107-6110.
3. R. Hu, J. Luo, H. Wen, C. Liu, J. Peng, Z. Xiong, D. Wang, Z. Feng, Y. Peng and R. Che, *Adv. Funct. Mater.*, 2024, **35**.
4. N. Qu, G. Xu, Y. Liu, M. He, R. Xing, J. Gu and J. Kong, *Adv. Funct. Mater.*, 2024, **35**, 2402923.
5. L. Meng, Y. Ma, Y. Zou, G. Chen, C. Dong and H. Guan, *J. Alloys Compd.*, 2024, **976**.
6. J. Tao, L. Xu, C. Pei, Y. Gu, Y. He, X. Zhang, X. Tao, J. Zhou, Z. Yao, S. Tao and H. Wu, *Adv. Funct. Mater.*, 2022, **33**.
7. B. Fan, R. Ji, Y. Yu, B. Huang, G. Tong and W. Wu, *Carbon*, 2024, **228**.
8. L. Duan, J. Zhou, Y. Yan, J. Tao, Y. Liu, Y. Lei, K. Zou, Y. Wang, H. Huang, X. Tao, P. Liu, Y. Ma and Z. Yao, *Adv. Funct. Mater.*, 2024, **35**, 2416727.
9. P. Chen, S. He, Z. Zou, T. Wang, J. Hu, J. Tao, L. Yang and Y. Li, *Adv. Funct. Mater.*, 2025, 2506308.
10. C. Gao, D. Gou, G. Huang, Z. Zhang, J. Wei, F. Gao, Y. Zhang, M. Terrones, X. Chen and Y. Wang, *Nano Energy*, 2025, **138**.

11. F. Pan, K. Pei, G. Chen, H. Guo, H. Jiang, R. Che and W. Lu, *Adv. Funct. Mater.*, 2023, **33**, 2306599.

12. C. Liu, Y. Cai, T. Liang, T. Zang, G. Fei and H. Xia, *Chem. Eng. J.*, 2025, **520**, 165717.

13. S. Zheng, W. Xu, J. Liu, F. Pan, S. Zhao, Y. Wang, Z. Zeng and N. Wu, *Adv. Funct. Mater.*, 2024, **34**, 2402889.

14. L. Wu, G. Wang, S. Shi, X. Liu, J. Liu, J. Zhao and G. Wang, *Adv. Sci.*, 2023, **10**, 2304218.

15. M. Anjali, K. Rengaswamy, A. Ukey, L. Stephen, C. V. Krishnamurthy and V. Subramanian, *Journal of Applied Physics*, 2023, **133**, 063105.

16. X. Zhang, X. Ma, J. Dang, X. Liu, X. Chen, H. Li and B. Cai, *Appl. Surf. Sci.*, 2026, **717**, 164774.

17. X. Hu, Y. Zhou, Y. Li, C. Ye and M. Zhu, *Chem. Eng. J.*, 2025, **516**, 164292.

18. B. Zhang, J. Cui, D. He, J. Zhang, L. Yang, W. Zhu and H. Lv, *J. Mater. Sci. Technol.*, 2024, **185**, 98-106.

19. R. Zhou, H. Zhang, S. Xu, L. Deng, C. Hu, F. Cao, S. Ali, Y. Guo, X. Mu, S. Zhao and X. Jian, *J. Alloys Compd.*, 2025, **1022**, 179935.